JOURNAL OF MATERIALS SCIENCE 25 (1990) 3541–3545

Microstructure and thermal stability of a rapidly solidified Al–4Er alloy

A. RUDER, D. ELIEZER
Department of Materials Engineering, Ben-Gurion University of the Negev, Beer-Sheva, Israel

The effect of the rapid-solidification melt-spinning process on an Al–4Er alloy has been studied. Compared to the normally solidified master alloy, rapid-solidification processing promotes the formation of a eutectic suppressed, relatively refined microstructure. Varying relative proportions of microstructures occupy the ribbon longitudinal transverse cross section: the featureless zone at the contact surface, the columnar zone in the middle and the equiaxed grains zone with degenerated dendrites at the free surface. The presence of a finely dispersed, coherent Al_3Er secondary equilibrium phase in the contact is evident. Ribbon microhardness remains fairly stable up to 200° C and at further elevated temperatures retains higher mean values than the master alloy.

1. Introduction

The role of strengthening additive elements from the lanthanide group for aluminium and aluminium alloys is at the focus of some current research [1–4]. Introducing rapid solidification (RS) techniques to increase the thermal stability of aluminium and aluminium alloys is considered a promising processing route. One of the general strategies involves internal formation of hard and stable intermetallic compounds in an aluminium matrix.

Due to the prospect of dispersoids and/or supersaturated refined microstructure formation [5, 6] via RS processing, improved mechanical and thermal stability properties in aluminium rare-earth (RE) alloys are assumed. The Al–Er equilibrium binary system [7] tends to form, on the aluminium-rich side, a high-melting-temperature intermetallic compound. The limited solid solubility of solute, high solubility in the liquid and the relatively low solid-state diffusivity of RE elements in an aluminium matrix suggest that this system (as well as other Al–RE systems) is a suitable lightweight, dispersion-strengthened alloy candidate for elevated homological temperature applications.

2. Experimental procedures

Ribbons from a nominal aluminium–4 wt % erbium master alloy were prepared by the melt-spinning technique in conditions described elsewhere [4]. The ribbon received has ~3 mm on ~0.07 mm cross-section average dimensions.

Samples cut from the continuous ribbon were heat treated for 2 h at 100, 200, 300, 400 and 500° C in an argon protective atmosphere and were designated at T1 to T5, respectively. Samples in the as-received condition and the master alloy were designated as T0 and MA, respectively.

Specimens were subjected to scanning electron microscopy (SEM) and electron dispersion of X-ray (EDX) examination and analysis, and scanned in the following different positions and conditions:

T0, T1, T2, T3, T4 and T5; longitudinal transverse cross section, mounted in a "cold" acrilic resin, polished only down to 1 μm alumina powder, polished and then etched with a standard Keller solution.

MA from the original master alloy, thin polished and then polished and etched, ~20 × 10 × 3 mm slices.

For transmission electron microscopy (TEM) studies, ϕ3 mm specimens were punched from the T0 ribbon for sample-holder mounting. Locations in the specimen transparent to the electron beam were examined. In general, the contact surface was kept perpendicular to the incident electron beam. Samples were studied at room temperature.

From mechanically thinned MA pieces, punched specimens were taken for TEM studies. Following controlled electrochemical polishing, the samples were further thinned for TEM examination.

X-ray diffractometry (XRD) was performed on the T0, T1, T2, T3, T4 and T5 ribbons. Using an amorphous adhesive spray, short pieces (25 mm) from these ribbons were respectively glued to a glass slide, with the contact surface in direct exposure to the X-ray beam. The exposed area was equal for all samples. Relatively thick, flat and polished pieces from the MA were also X-rayed in the same conditions as the ribbons.

Knoop microhardness measurements were made on three samples taken from each thermal condition and from the MA. Readings were obtained from resin-mounted, longitudinal transverse, polished cross sections, at zones near the contact surface, mid-ribbon and near-free-surface locations, 15 indents per sample (45 indents per thermal condition). The long axis was kept parallel to the long dimension of the ribbon, with a 10 g load and 10 sec dwell time. The polished MA was indented 15 times at random locations.

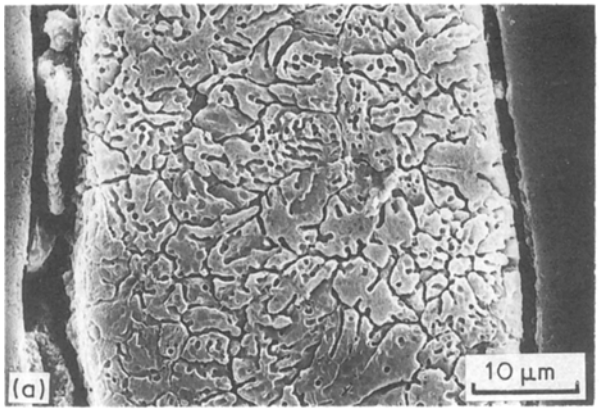

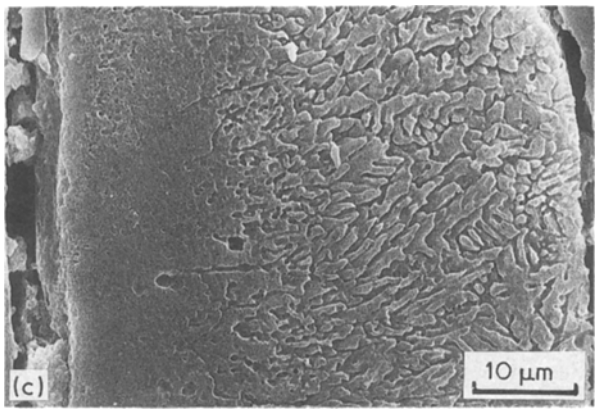

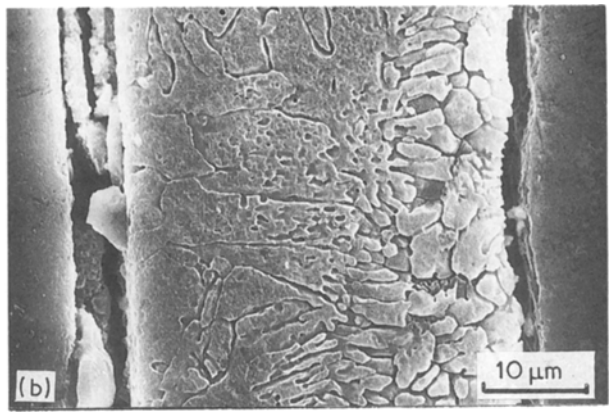

Figure 1 SEM longitudinal transverse cross-section micrographs of the ribbon, T0 condition, with the three distinct types of micromorphology. Contact surface is on the left.

3. Results and discussion

SEM micrographs indicate that the ribbon's longitudinal transverse cross sections (Figs 1a–c) is occupied in varying relative proportions by three distinct types of micromorphology:

(i) a featureless zone adjacent to the contact surface;

(ii) a columnar structure having a deflected transient interface; and

(iii) equiaxed grains having a degenerated dendritic substructure closing from the interface up to the free surface.

The different types and relative proportions of micromorphologies, as observed across the ribbon's smallest dimension, arise from varying solidification rates across the ribbon. These variations are probably due to the local fluctuations in conditions during the manufacturing process, variations in contact efficiency between ribbon and wheel, non-uniform liquid metal supply, and others. These varying solidification rates, result in the formation of a mixed mode of micromorphologies.

Using the spacing and cooling-rate relationship derived from a few aluminium alloys [8]

$$\lambda = \beta\varepsilon^{-n} \quad (1)$$

where λ = spacing/cell size (μm); ε = cooling rate (K sec^{-1}); $\beta = 50\,\mu$m (K sec^{-1})$^{1/3}$; and $n = \sim 0.3$, the calculated local cooling rate in the 0.5 μm degenerated dendrite arm spacing was about 10^6 K sec^{-1}. This result is in agreement with the calculation based on the relationship of ribbon dimensions to casting conditions [9], where the solidification time, Θ(sec), is

$$\Theta = X/V \quad (2)$$

where X = distance from the 'nose' of the puddle to the solidification point (cm); and V = speed of the chill surface (cm sec^{-1}). The solidification time based on $X = \sim 0.5$ cm, $V = 2240$ cm sec^{-1} is

$$\Theta = \sim 2.2*10^{-4}\ \text{sec} \quad (3)$$

and the overall average calculated, 100 K overheat, cooling rate is

$$\varepsilon = \sim 5*10^5\ \text{K sec}^{-1} \quad (4)$$

The featureless zone can be related to even higher cooling rates (near the contact) as compared to the calculated cooling rates, which resulted in the formation of the columnar and equiaxed structures, respectively. The origin of the deflected transient is in the accelerating forces instantaneously acting on the puddle during contact with the rotating chill. Similar cross-section structures have been observed in RS, melt-spun Al–11.6 wt % Er alloy [4], suggesting that the microstructure resulting from similar cooling rates is not composition-dependent.

The fact that no measurable shifts in the aluminium matrix XRD intensity peaks of the diffracted ribbons were observed suggests negligible erbium solid-solution miscibility in the aluminium matrix. Such miscibility would have resulted in an expanded aluminium lattice parameter, inducing shifts in the aluminium matrix diffraction-pattern peaks. The other intensity peaks originate from the erbium-rich phases only, identified as the (finely dispersed) Al_3Er equilibrium phase. Following heat treatments, coarsening of the Al_3Er phase results in narrow XRD intensity peaks of this phase, but the intensity does not change. This indicates that the total amount of the Al_3Er phase remains constant and is not affected by the various heat treatments.

The XRD patterns of the MA and the ribbons are similar in terms of presence and identification of the two phases, but differ in intensity, mainly because the area size of the MA exposed to the X-ray beam was not equal to the area size of the X-rayed ribbons.

Erbium EDX macroconcentration along the cross section, in T0, T3, T5 only in the polished condition, as shown in Fig. 2, varies from contact surface to free surface and stands on lower values than the nominal

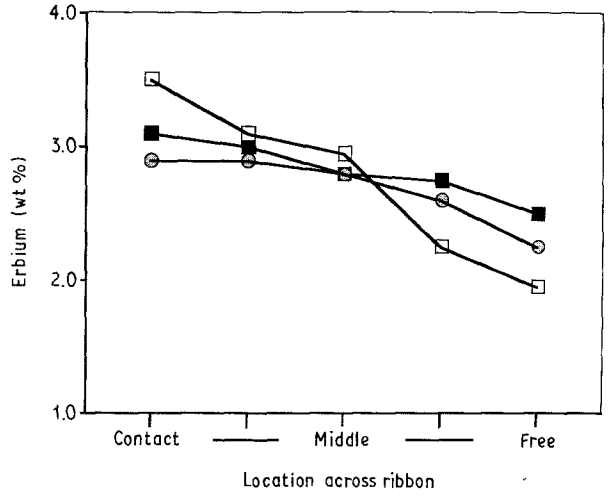

Figure 2 Erbium EDX concentration profiles across polished-only ribbon in □, T0; ■, T3 and ○, T5 condition. (The solid lines connecting data points are drawn for convenience only.) RS, Al–4Er. Standard deviation ±0.3 wt %.

4 wt % Er concentration. These variations are respectively related to instrumental limitations in processing the EDX spectra by raising aluminium concentration as the aluminium major spectral line overlaps one of the erbium minor spectral lines, resulting in lower than nominal erbium concentration values for each reading. The more homogeneous distribution of the Al_3Er phase near the contact and low grain boundary density shows relatively higher erbium concentration values in this zone when compared to the near-free-surface zone. In the near-free-surface zone, the Al_3Er phase is not homogeneously distributed, mainly along grain boundaries. XRD examination of this zone results therefore in lower erbium concentration readings.

It can also be assumed (Fig. 2) that the present heat treatments have negligible influence on erbium distribution in the RS bulk.

Erbium macroconcentration varies considerably across polished and etched ribbons, with relatively high values in the contact zone and low values in the free-surface zone. These variations can be related to selective etching that removes the erbium-rich phase mainly from grain boundaries. As grain boundaries act as segregation sinks, higher amounts of erbium or erbium-rich phase, not trapped in the matrix during a slower solidification process, migrate to the relatively dense grain-boundary-line zone near the free surface. The following selective etching removes the grain-boundary erbium-rich phase, resulting in a lower erbium concentration at locations adjacent to the free surface. But the concentration is still higher than dictated by the phase diagram, indirectly indicating the presence of the erbium-rich phase within the aluminium matrix.

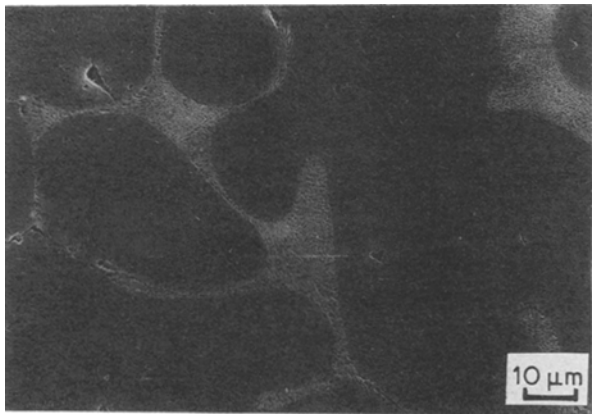

Figure 3 SEM micrograph of the polished and etched Al–4Er master alloy (MA).

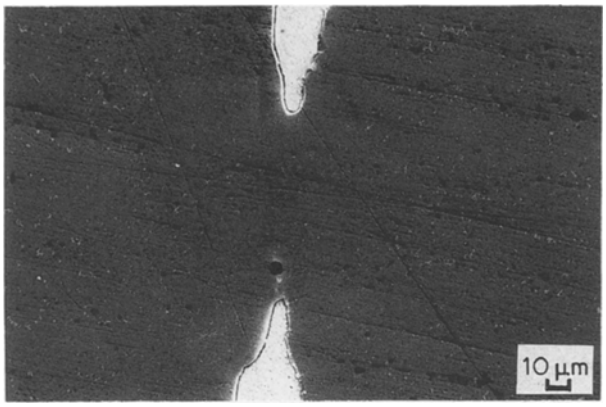

Figure 4 SEM micrograph of an as-received discontinuity in a cross-sectioned ribbon. Similar locations were used in TEM studies.

The MA microstructure is a typical, equilibrium-solidified binary Al–4Er casting that has an expected phase and constituent distribution, clearly different from the RS products. A SEM micrograph taken from the polished and etched MA (Fig. 3) shows a rounded, elongated grain structure and a heavy intergranular structure of a fine lamellae eutectic. The erbium EDX overall average macroconcentration taken from an only polished MA was 3.2 wt % Er. Erbium concentration in grain centres was nil (under the resolution of the present EDX), while in the eutectic it was at an average of 8.6 wt % Er.

Fig. 4 shows an as-received discontinuity in the ribbon's transverse cross section. Similar locations, transparent to the TEM electron beam, were studied. Being adjacent to the contact surface, these thin, transparent locations probably undergo the highest cooling rates.

Figs 5a and b show, respectively, bright- and dark-field TEM images of an as-received transparent location. The finely dispersed, round cross-section particles were identified as the cubic Al_3Er phase. Orientation relationships between the matrix and the dispersed phase derived from the results in Figs 5a, c and 6a are $\{100\}_{Al_3Er} \| \{100\}_{Al}$; $\langle 100 \rangle_{Al_3Er} \| \langle 100 \rangle_{Al}$. Contrast parallel fringes can be observed in Fig. 6b. The moiré fringe contrast arises from the two superimposed lattices of slightly different spacing and/or orientation. For parallel contrast lines, the moiré spacing D is given [10] as

$$D = d_1 d_2 / (d_1 - d_2) \quad (5)$$

where: d_1, d_2 = the relevant lattice plane spacing of the matrix and the precipitate. The construction necessary to obtain the relevant planes is shown in Figs 6a and b. The calculated moiré D spacing with

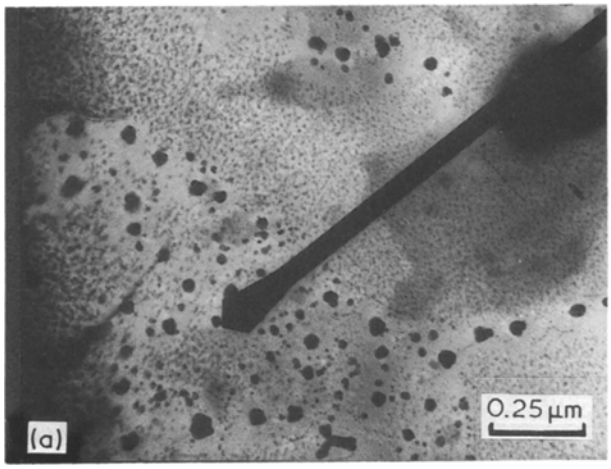

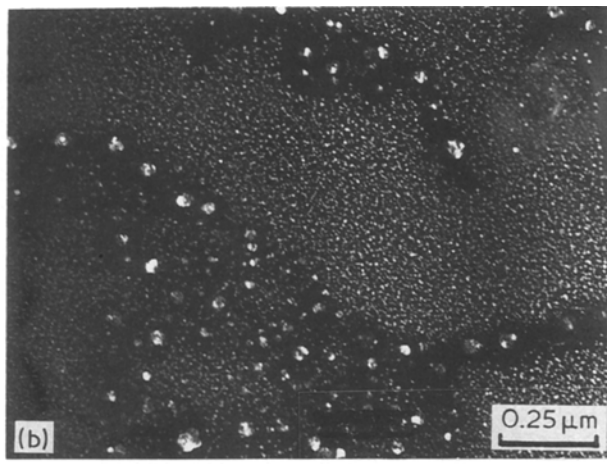

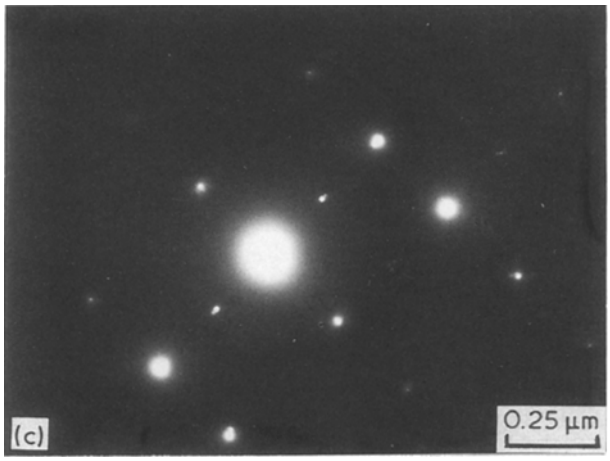

Figure 5 TEM micrographs of a transparent location in the ribbon: (a) bright field selected area; (b) dark field, the same selected area as in (a); (c) diffraction pattern from (a).

the relevant matrix and precipitate planes is as follows:

$$d_{(3\,1\,1)Al_3Er} = 0.1270\,\text{nm}$$

$$d_{(3\,1\,1)Al} = 0.1221\,\text{nm}$$

$$D = 3.1600\,\text{nm}$$

At a $4*10^4$ magnification, the calculated D spacing is expected to be 0.13 mm on the photographic plate. The actual (measured) D spacing is ~ 0.15 mm, in high agreement with the calculated result.

TEM studies of the MA show that the Al_3Er phase is not dispersed in the aluminium matrix and is located in the eutectic structure, along grain boundaries only. A typical MA, TEM bright field image is presented in Fig. 7.

Microhardness test results are summarized in Fig. 8. The ribbons maintain higher relative hardness values up to T4 condition, when compared to the MA. The hardness of a T0, Al–4Er mid-ribbon, is lower than the as-cast Al–11.6Er mid-ribbon [4], emphasizing alloying influence on hardness, probably by the formation of a denser strengthening secondary phase in the Al–11.6Er alloy.

The hardness readings taken from the contact, mid-ribbon and free-surface zones do not differ substantially from one another, and are fairly stable up to the T2 condition. A relatively sharp decrease in hardness, regardless of location, is observed in ribbons treated at temperatures above 200° C. From this behaviour the following assumptions can be made. The combined influence of the finely dispersed secondary phase in the refined microstructure acts as a strengthening medium, resulting in a relative increase in hardness. This influence is more evident at the near-contact-surface zone, where even more refined microstructures are observed. Also, due to coarsening of the secondary phase, a sharp decrease in relative hardness between the T2 and T5 conditions is observed.

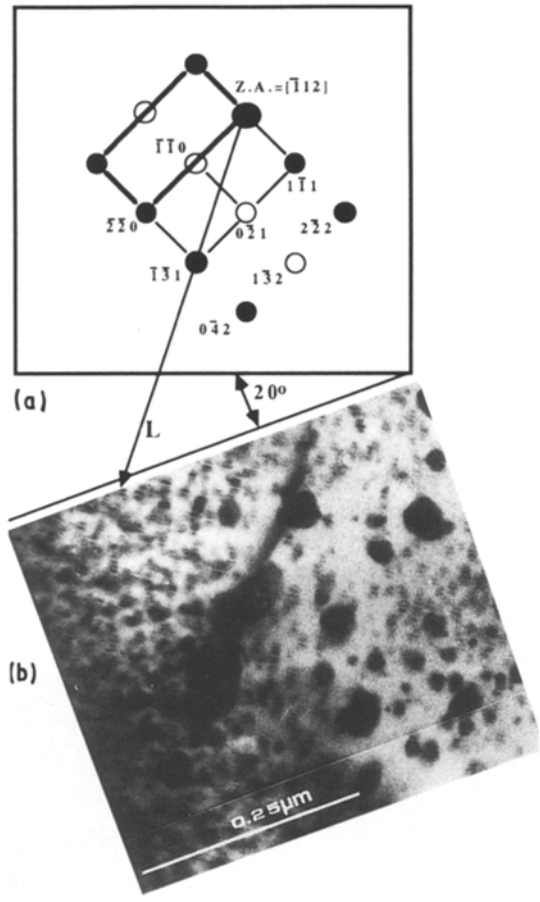

Figure 6 A combined construction for the determination of moiré fringe spacing: (a) TEM relevant indexed diffraction pattern (from Fig. 5c). •, Aluminium matrix indexed diffraction pattern; ○, Al_3Er indexed diffraction pattern; ●, central beam. ZA, aluminium and Al_3Er zone axis. 20°, Respective angle between the TEM image and the relevant diffraction pattern. L←, Line running through the plane intensity spot which is perpendicular to the relevant moiré fringes. (b) TEM micrograph, bright-field image (enlarged section from Fig. 5a). Parallel fringes are within particle-image boundaries.

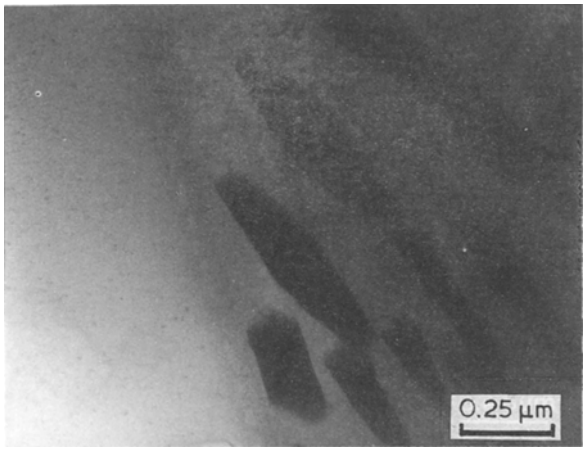

Figure 7 TEM micrograph, bright-field image from the MA, eutectic microstructure embedded in a particle-free grain boundary.

4. Summary and conclusions

RS processing promotes the formation of featureless, eutectic-free, relatively finer microstructures in an Al–4Er alloy, clearly different from the MA. The mixed mode of microstructures across the RS ribbon is related to local fluctuations during alloy RS processing, when the calculated average overall cooling rate was in the range $\sim 10^5$ to 10^6 K sec^{-1}. The formation of a finely dispersed Al_3Er secondary equilibrium phase is the result of RS processing. A specific orientation relationship between the aluminium matrix and the Al_3Er dispersoids has been established. The RS alloy stability, as expressed in terms of microhardness, is almost unchanged up to 200° C at 2 h exposure, and is related to the presence of the finely dispersed Al_3Er secondary equilibrium phase.

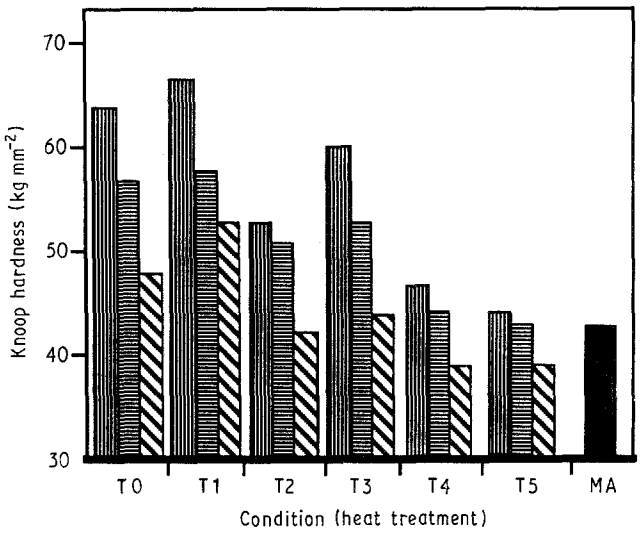

Figure 8 Knoop average microhardness results from the MA and from heat-treated, longitudinally cross-sectioned ribbon at near-contact-surface, mid-ribbon and zones near the free surface. ▩, contact; ▤, mid-ribbon; ▧, free. S.D. for T0 to T3, ± 7.0 kg mm^{-2}; for T4, T5 and MA, ± 5.0 kg mm^{-2}.

Acknowledgements

The authors would like to thank Dr F. H. Froes and the Air Force Wright Aeronautical Laboratories, Wright–Patterson AFB, Dayton, Ohio, USA, for providing the alloys, and Dr. E. Manor for helpful discussions of the TEM results.

References

1. J. W. ZINDEL, D. C. VAN AKEN, R. D. FIELD, P. KURATH and H. L. FRASER, in "Mechanical Behaviour of Rapidly Solidified Materials", edited by S. M. L. Sastry and B. A. MacDonald (Metallurgical Society, Warrendale, Pennsylvania, 1985) p. 189.
2. A. K. GOGIA, P. V. RAO and J. A. SEKHAR, *J. Mater. Sci.* **20** (1985) 3091.
3. Y. R. MAHAJAN and S. D. KIRCHOFF, *Scripta Metall.* **20** (1986) 643.
4. S. J. SAVAGE, F. H. FROES and D. ELIEZER, in "Rapidly Solidified Materials", edited by P. W. Lee and S. Carbonara (American Society of Metals, Ohio, 1985) p. 351.
5. H. JONES, *Mater. Sci. Engng* **5** (1969/70) 1.
6. R. MEHRABIAN, *Int. Met. Rev.* **27** (1982) 185.
7. K. A. GSCHNEIDNER and F. W. CALDERWOOD, "Critical Evaluation of Binary Rare Earth Phase Diagrams" (Iowa State University, Ames, 1983) p. 498.
8. H. JONES, "Rapid Solidification of Metals and Alloys", Monograph No. 8 (Institute of Metallurgists, London, 1982) p. 42.
9. S. KAVESH, "Rapid Solidification Technology – Source Book", edited by R. L. Ashbrook (American Society of Metals, Ohio, 1983) p. 73.
10. G. W. LORIMER, "Electron Microscopy and Microanalysis of Crystalline Materials", edited by J. A. Belk (Applied Science, London, 1979) p. 34.

Received 15 March
and accepted 30 August 1989